# Carrier Density Non-pinning at Stripe Edges and Widened Lateral Far field due to Longitudinal Temperature Variation in Broad-Area High Power Diode Lasers

**S. K. Khamari[1†], S. Arslan[†], C. Zink[†], S. J. Sweeney*[†] and P. Crump[†]**

[†] *Ferdinand-Braun-Institut (FBH), Gustav-Kirchhoff-Str. 4, 12489 Berlin, Germany*

**James Watt School of Engineering, College of Science and Engineering, University of Glasgow, Glasgow, G12 8LT, UK*

[1]*Author e-mail address: Shailesh.Khamari@FBH-Berlin.de*

## Abstract

Broad area lasers operating at high power with improved beam quality are needed in many applications. In typical high-power diode lasers with asymmetric facet coating, it is observed that the carrier density fails to completely pin above threshold with significant levels of lateral carrier accumulation (LCA) at the front facet stripe edges. Systematic experimental data are presented to quantify such non-pinning and its effect on lateral far field in multiple diode lasers with varying longitudinal temperature variation (LTV) using spontaneous emission imaging. LTV is quantified and correlated to the carrier accumulation and its dependence on facet reflectivity and cavity length. Results of measurements under continuous wave (CW) and quasi-CW conditions are used regulate the level of heating and hence to isolate the contribution of LTV and optical field profile. Conventional long resonator asymmetric-coated devices show twofold increase in LCA from threshold to 10 A current at the front stripe edge, but LCA varies less than 20% for lower facet asymmetry or short resonators. Similarly, strong temperature driven far field broadening is observed for conventional long-resonator asymmetric-coated devices (3…4° variation with temperature at 10A), which is strongly reduced for lower facet asymmetry or short resonators (< 1° at 10 A).

Due to high electro-optical conversion efficiency ($\eta_E$) and high-power ($P_{out}$), GaAs based broad area lasers (BAL) with operating wavelength 9xx nm are well established tools for a variety of industrial and medical applications.[1] Though continuous efforts have been made to improve the output power and beam quality in these lasers, they generally exhibit early power saturation and rapid increase in lateral beam parameter product ($BPP_{lat}$) known as 'far field blooming'.[2] The root cause of this process has been examined intensively both experimentally and theoretically, e.g., in Ref. 3 and references therein. Among other contributions, spatial non-uniformity in the optical field, temperature and carrier density are considered to be major limits to $P_{opt}$ and $BPP_{lat}$. Generally, high-power devices have deliberate asymmetry in their facet reflectivities to ensure maximum coupling of the output power with optical systems. At high drive current, this results in a strong variation in the optical field along the resonator leading to large variation in local gain and carrier density degrading threshold current,[4,5] internal differential efficiency and their temperature dependence.[6] This also results in strong longitudinal variation of temperature (LTV), with higher temperatures predicted to occur at the front facet, which ultimately leads to the high current flowing near the front facet of BAL[7,8]. It has also been shown that the strong thermal lens at the front facet leads to narrowing of the near field and broadening of the far field at the front facet.[9] On the other hand, because of a flatter optical field profile, equalizing the facet reflectivities increases the total power (out of both facets) and reduces the thermal contribution to the lateral far field (LFF).[10] It is predicted that the narrowing of the near field results in carrier density non-pinning effects, with higher carrier

densities accumulating at the stripe edges.[9,11] In a recent study, such lateral carrier accumulation (LCA) is confirmed by spontaneous emission imaging and correlated with the onset of high current flow and hence higher recombination rates in this region.[12] However, its evolution with active zone temperature variation is not found in available literature. In this letter, we report on an expanded experimental investigation of carrier accumulation at the stripe edge, its dependence on longitudinal inhomogeneity and its impact on lateral beam quality. Here, the longitudinal inhomogeneity is induced in the cavity either during fabrication by varying the rear and front facet reflectivity ($R_r$ and $R_f$) and by varying the cavity length ($L$) or during measurements by varying the drive current (I). The experiments are conducted using continuous wave (CW) and pulsed mode (quasi-CW) conditions to separate the overall impact of temperature and optical field profiles on LCA and lateral far field angle, $\theta_{95\%}$ (for 95% power content). We show in this study that as the LTV reduces either by increasing $R_f$ or by decreasing $L$, LCA and $\theta_{95\%}$ reduce confirming finite correlation between them. The article is structured as follows. First, we have quantified the carrier accumulation at the stripe edges of laser diodes having different LTV, which is determined from the imaging of spontaneous emission intensity in the plane of the quantum well. The measurements are further repeated under quasi-CW conditions, where the average cavity temperature is tuned at a constant bias by varying pulse width and repetition rate and compared with CW conditions, where longitudinal variation is tuned by changing the bias level. Next, the lateral far field distribution for the same devices is measured under identical experimental conditions (CW and quasi-CW) and correlation is made with carrier accumulation, before concluding.

The devices considered in this work make use of an asymmetric large optical cavity design with an InGaAs single quantum well as active region surrounded by AlGaAs cladding layers, and are grown by metal-organic vapor phase epitaxy, as detailed in Ref.[13] These edge emitting devices operating at around 970 nm are fabricated with stripe width $W$ = 90 µm, and $L$ = 3 mm and 6 mm. In addition, a window of width 140 µm was opened on the substrate side by removing the metallization over the laser stripes using lift-off techniques (Fig. 1 (a)). After cleaving, the facets of the bars are passivated using ZnSe and are coated with dielectrics to obtain the required reflectivity. Three sets of samples with different construction are considered to regulate the levels of LTV and LCA, with two devices in each set to assess reproducibility. The first set of devices (D1 and D2) use a conventional device configuration for maximum coupling of power out of the front facet and hence are extremely asymmetric having cavity length ($L$) of 6 mm and $R_f$ = 0.8 %, where strong longitudinal variation has previously been seen.[12,13] In the second set (D3 and D4), $R_f$ is increased to 20 %, thereby considerably flattening the optical field (predicted to be flat) and hence temperature and carrier profile. In the third set (D5 and D6), $L$ is reduced to 3 mm, keeping $R_f$ similar (1%). All the devices have $R_r$ = 98%. The details of the devices are summarized in Table 1. The bars are further cleaved into single elements and soldered epi-down using Au-Sn on expansion matched CuW (10:90) carriers and then mounted on a conduction cooled package (CCP). This configuration, allows the spontaneous emission from the quantum well to be detected, as the GaAs substrate is transparent beyond 870 nm. The output power is measured using a calibrated thermoelectric detector. For L= 6 mm devices, voltage across the diodes is measured using the four-probe method. On the other hand, for L = 3 mm devices, it is measured in 2-probe configuration. Subsequently, the estimated voltage drop across the series resistance originating from the package is subtracted to evaluate the voltage across the diode. The packaged devices are

mounted on a heat sink coupled with a XYZ translation stage and all the experiments are conducted at 20 °C, unless otherwise stated.

Table 1. Details of device parameters and important experimental findings. The symbols are explained in the text.

| **Set** | **Device** | $L$ (mm) | $R_f$ (%) | $S_{edge}/S_{center}$ | $\theta_{95\%}/\Delta T_{AZ}$ (deg/K) |
|---|---|---|---|---|---|
| 1 | D1 | 6 | 0.8 | 1.9 | 0.16 (±0.01) |
| | D2 | 6 | 0.8 | 2.0 | 0.14 (±0.01) |
| 2 | D3 | 6 | 20 | 1.15 | 0.04 (±0.01) |
| | D4 | 6 | 20 | 1.15 | 0.07 (±0.007) |
| 3 | D5 | 3 | 1 | 1.15 | 0.06 (±0.008) |
| | D6 | 3 | 1 | 1.14 | 0.07 (±0.009) |

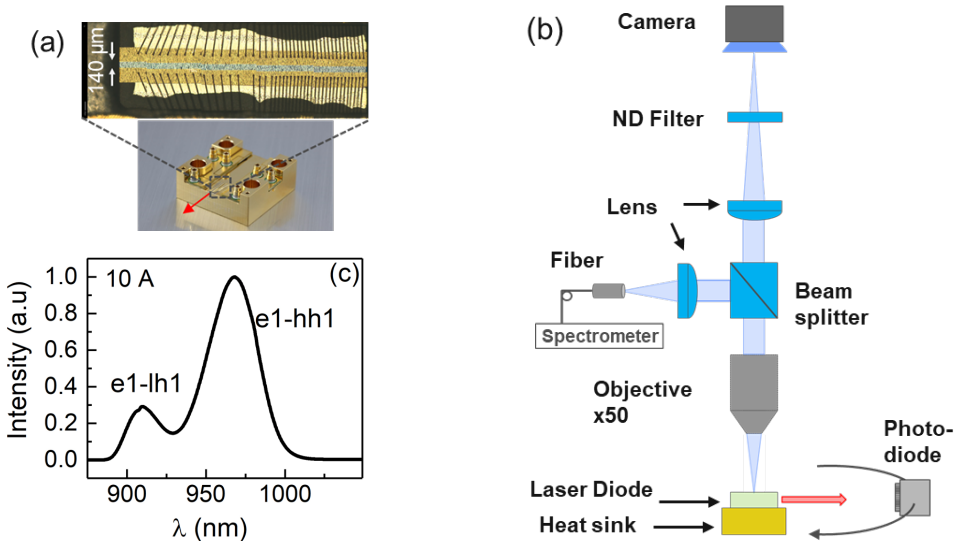


***Fig. 1****(a) Mounted device with expanded view showing the substrate-side metallization window (b) Experimental setup used in this work. (c) Typical luminescence spectra collected from one of the devices (D1) at 10 A, showing the peaks corresponding to e1-hh1 and e1-lh1 transitions.*

Figure 1(b) shows the schematic diagram of the experimental setup used for the measurements. The spontaneous emission is collected using a 50x microscope objective and further divided using a 50% / 50% beam splitter cube. Using collection optics, this is then delivered to a CMOS camera and high-resolution spectrometer for spatial and spectral analysis, respectively. [12] The spectrally and spatially integrated spontaneous power ($P_{SP,}$ integrated over an area of 140 µm diameter) is measured with a Keysight 8163B lightwave multimeter. The CMOS camera can capture an image of 450 µm x 450 µm in a single frame and the devices are translated along the longitudinal axis to capture images along the whole cavity. Careful alignment also minimizes the contribution of scattered stimulated emission in the spontaneous

emission spectra, as evidenced from the Fig. 1(c), where, a typical spontaneous emission spectrum collected above threshold is depicted. The test station is further equipped with a goniometer setup (Fig. 1 (b)) to analyse both the lateral and vertical far field distribution with an angular resolution of 0.1 deg.

Figure 2 (a) shows the CW electro-optical performances of the devices of each set, confirming high $\eta_E$ for conventional Set 1 (6 mm, 0.8%) and Set 3 (3 mm, 1%) devices, with lower values for Set 2 (6 mm, 20%). In Fig. 2 (b) and (c), the longitudinal variation of spontaneous emission wavelength and total spontaneous emission power $P_{sp}$ (for > 870 nm) at 10 A are plotted. The estimated LTV is also plotted, estimated from the spectral shift of the luminescence spectrum assuming a temperature sensitivity of 0.3 nm/K. Following Ref. [11], the spectral shift with changes in carrier concentration is neglected to a first approximation. Carrier density (not shown) can be estimated from the measured $P_{SP}$, assuming a temperature and carrier-density-independent bimolecular recombination coefficient, $B$, using the approximation $n = p$, from $P_{SP} \propto Bn^2$. In an ideal QW laser, $B \propto T^{-1}$ and is independent of $n$ [14], consequently, within the small (< 5 K) expected variation of temperature and carrier density, this can be considered a reasonable first approximation. It should be noted that, the average temperature of the cavity is higher for 3 mm devices because of their higher thermal resistance. Furthermore, because of the lower efficiency, the average temperature of the devices with $R_f$ = 20% is higher than that of the devices with $R_f$ = 0.8%. Therefore, to compare the temperature inhomogeneity among the devices, the difference between estimated local temperature and minimum temperature within the active zone ($\delta T_{AZ}$) is plotted as a function of longitudinal position in Fig. 2(b). It is clearly observed that the temperature at the front facet is higher than at the back facet in all the devices, confirming the presence of LTV. Further, magnitude of LTV in D1 is more than twice that in D3 and D5. Though only one device per set is included in the plot, LTV is similar for both the devices within the same set. A similar observation is also seen in terms of carrier density in Fig. 2(c), where $P_{SP}$ is plotted as a function of longitudinal position. It should be noted here that $P_{SP}$ is measured from an area of 140 µm diameter using a power meter. Thus, the laser diode mounted on translation stage has to be moved after each measurement, which can potentially cause variation in coupling of spontaneous emission into the collection optics.[13] However, this effect is minimized by normalizing the measured intensity at 10 A with respect to that measured below threshold (0.5 A), where the carrier density is essentially uniform. Owing to longitudinal spatial hole burning, the carrier density becomes much higher at the rear facet as compared to the front facet. Considering the temperature-induced modification of refractive index ($d\mu/dT = 3 \times 10^{-4}\ K^{-1}$), its variation between front and back facet is estimated to be $1.35 \times 10^{-3}$, $5.7 \times 10^{-4}$ and $5.1 \times 10^{-4}$ for D1, D3 and D5, respectively at 10 A.[15] Note that here we assume that the carrier density induced modification of refractive index is negligible as compared to $d\mu/dT$. [15]As the applied current reduces, the longitudinal variation of both $\delta T_{AZ}$ and $P_{SP}$ reduces considerably. Thus, the longitudinal variation in the cavity can be tuned by tuning $R_f$, $L$, and $I$.

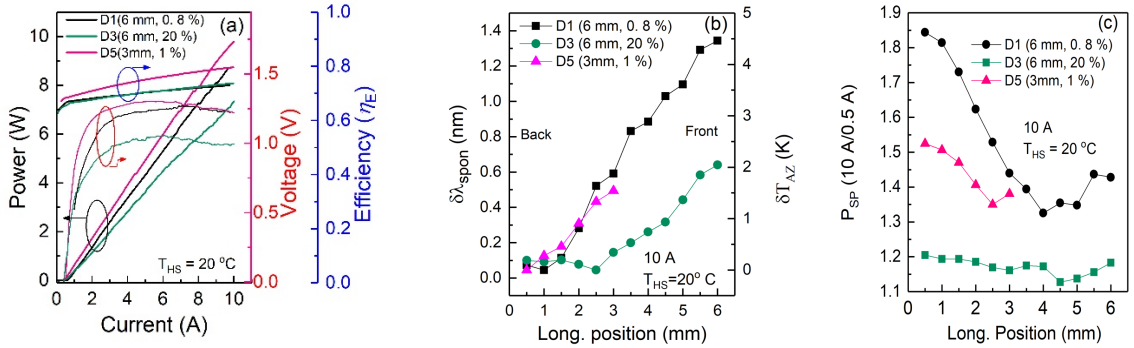


***Fig. 2*** *(a) CW electro-optical performance of three typical devices of each type. 10 A Longitudinal inhomogeneity in (b) active zone temperature and (c) $P_{SP}$. Here $\delta T_{AZ}$ is the difference between estimated local temperature and minimum temperature within the active zone.*

Once the magnitude of LTV and its dependence on applied current is quantified in all the three sets of devices, we turned our attention to the carrier distribution in the lateral direction. Figure 3 (a), (b) and (c) show the resulting map of spontaneous emission intensity in three devices (D1, D3 and D5) at 10 A applied current. Non-uniformity of carrier concentration across both longitudinal and lateral direction can be clearly seen in D1, which can be corroborated with that shown in Fig. 2 (c) establishing the consistency of the measurements. Lateral inhomogeneity is also seen in all the devices, though with different extent. In D3 and D5, small but finite accumulation is seen at the stripe edge, whose variation with longitudinal position is minimal. On the other hand, in case of D1, large accumulation is observed at the front facet only. Asymmetry in carrier accumulation is observed at the front facet with higher accumulation at one of the edges (here on the left side, also observed on the right side in other devices). This observation was confirmed in multiple devices and remains the subject of ongoing investigations.

This is clearly observed in Fig. 3 (d), where the 10 A lateral profile of spontaneous intensity at both the facets are plotted for the three devices. To quantify the LCA, we identified two parameters, which are marked by the horizontal line in Fig. 3 d. One is the peak spontaneous intensity, which is at the stripe edge ($S_{edge}$) and the other is the intensity averaged over 50 µm lateral dimension at the centre ($S_{centre}$). The ratio ($S_{edge}/S_{centre}$) is considered as a measure of front-facet LCA, which is found to be around 1.9, 1.15 and 1.14 for devices of set 1, 2 and 3, respectively, and is summarized in Table 1. A steady dependence of ($S_{edge}/S_{centre}$) on the applied current is observed in all the devices, as shown in Fig. 3 (e). Two devices each of the three sets are included to demonstrate the consistency. Since thermal lensing caused by the temperature difference between the active region and stripe edges is considered as one of the prime reasons of LCA, ($S_{edge}/S_{centre}$) is plotted against the average temperature rise in the active region ($\Delta T_{AZ}$), see Fig 3 (f). $\Delta T_{AZ}$ for each current is estimated from the shift of the centroid of the laser emission wavelength with respect to that measured for near threshold (1A), low duty cycle (0.5 %) operation. Considerable differences in the magnitude of $S_{edge}/S_{centre}$ between the devices in different sets are observed for the same $\Delta T_{AZ}$, e.g 18.3 K (corresponding to 10 A for D1), establishing the correlation between LTV and LCA. This is consistent with previous theoretical studies,[9] where the authors have calculated the optical field intensity and carrier density profile in the laser cavity for $L$ = 4 mm, $W$ = 120 µm, and $R_f$ = 2 %, both with and without LTV.

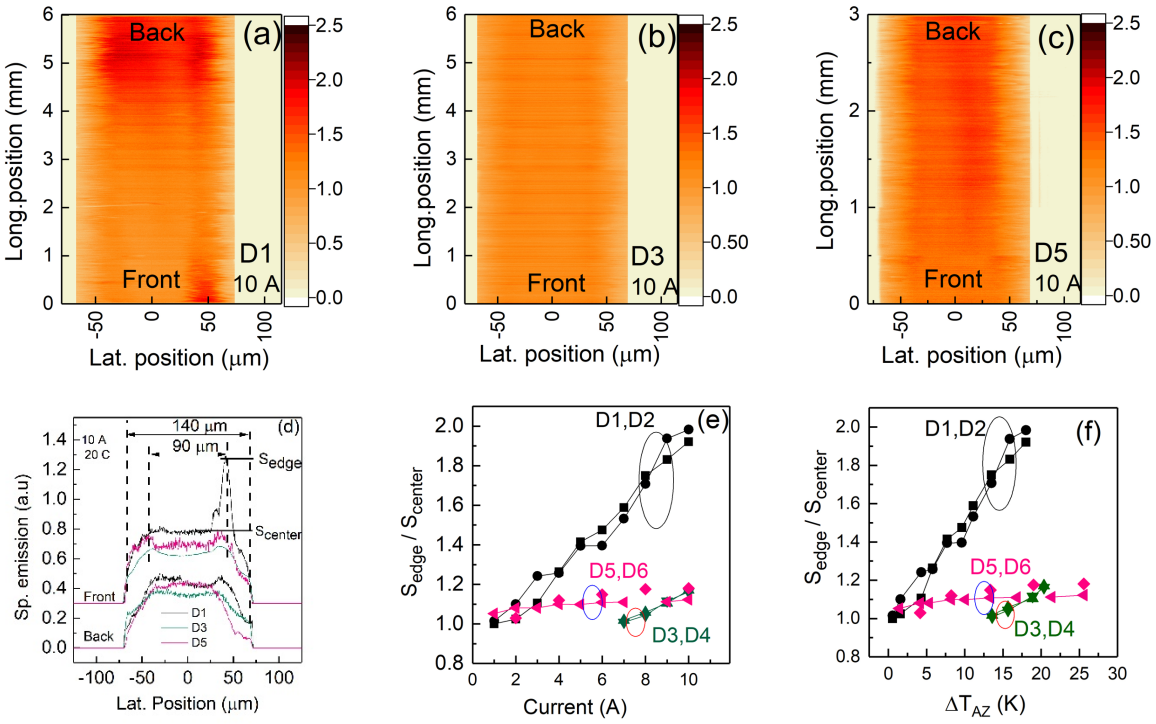


***Fig. 3**. Distribution of carrier density (a) D1 (b) D3 and (c) D5. (d) Lateral profile of carrier density at front and back facets. Profiles at front facet are shifted vertically. Variation of $S_{edge}$ / $S_{center}$ with (e) applied current and (f)* $\Delta T_{AZ}$.

It should be noted that increase in applied current not only increases $\Delta T_{AZ}$, but also increases the optical field intensity at the front facet leading to non-thermal mechanisms such as increasing carrier recombination above threshold especially at the device edges,[15] and current crowding at the front facet. [13] For this reason, we have systematically reduced self-heating by operating the devices under quasi-CW condition at a fixed applied current. The pulse width and frequency are varied between 100 μs to 800 μs and 100 Hz to 1 kHz respectively, tuning the duty cycle from 1 % to 80 %. All the measurements are performed in time-averaged mode. The measured values of ($S_{edge}/S_{centre}$) for D1 at 10 A (fixed current) is plotted in Fig. 4(a), where a significant variation with the pulse width and frequency is observed. It varies from 1.1 at 100 μs, 100 Hz (duty cycle 1%) to 1.8 at 800 μs, 1 kHz (80% duty cycle). To correlate these results with the temperature rise, ($S_{edge}/S_{centre}$) is plotted against $\Delta T_{AZ}$ in Fig. 4(b). The apparent scattered data in Fig. 4(a) converge into a single curve establishing the fact that ($S_{edge}/S_{centre}$) depends on $\Delta T_{AZ}$ and not on individual pulse width and frequency. Here, ($S_{edge}/S_{centre}$) is seen to be increasing with $\Delta T_{AZ}$ before saturating at the value obtained under CW condition (10 A). Such saturation can be attributed to gradual heating up of the regions outside the current stripe saturating the temperature gradient between the active region and its surrounding, confirming that front-edge LCA and non-pinning is thermally driven. The measurements are next repeated for identical quasi-CW condition at 6 A and similar saturation at high duty cycle is observed (Fig. 4(b)). A comparison of all three sets of devices is plotted in Fig. 4(c).

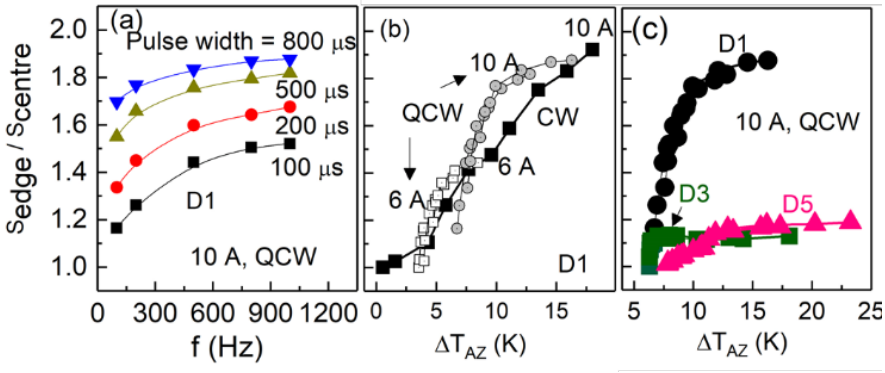


***Fig. 4.*** *$S_{edge}/S_{centre}$ for the D1 is plotted (a) for various pulse width and frequency. The lines are for eye guiding only and (b) as a function of $\Delta T_{AZ}$ (c) $S_{edge}/S_{centre}$ is compared for different sets of devices.*

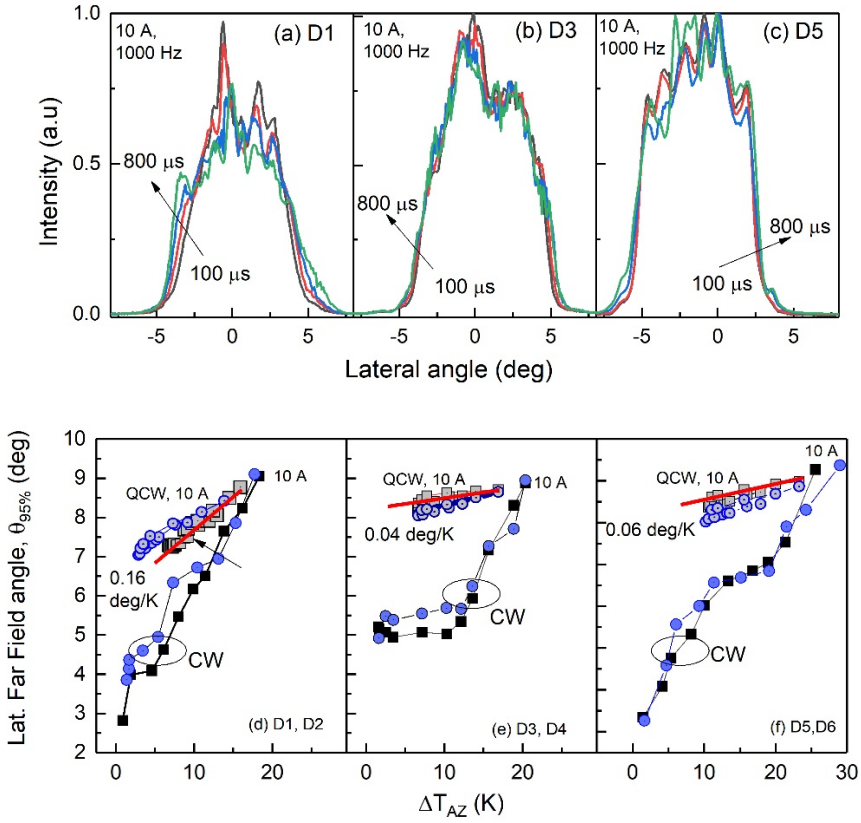


**Fig. 5.** Lateral far field profile for (a) D1, (b) D3 and (c) D5 for different pulse width at 1000 Hz frequency. $\theta_{95\%}$ as a function of active zone temperature under CW and quasi-CW operation for (d) D1, D2 (e) D3, D4 and (f) D5, D6.

The correlation between the carrier accumulation at the stripe edges with changes in the lateral far field distribution can be assessed by measuring the $\theta_{95\%}$, under identical CW and quasi-CW conditions. To this end, Fig 5 (a-c) depicts the lateral far field profile for the devices measured at 1000 Hz frequency and pulse width varying from 100 µs to 800 µs. Strong widening of the far field profile can be clearly seen in case of D1. As for the case of carrier accumulation, the estimated values of $\theta_{95\%}$ are plotted against $\Delta T_{AZ}$ in Fig 5 (d-f) for both CW and quasi-CW operation. The magnitude of $\theta_{95\%}$ increases with $\Delta T_{AZ}$ for all the measured

devices. At 10 A CW, the magnitude of $\theta_{95\%}$ is estimated to be 8.66 °, 8.86 ° and 9.26 ° for D1, D3 and D5, respectively, which is consistent with this general understanding that the lateral far field widens with self-heating. However, for the same variation in $\Delta T_{AZ}$, the variation in $\theta_{95\%}$ is considerably higher for D1 compared to D3 and D5. For example, at $\Delta T_{AZ}$ = 18.3 K for D1 (corresponding to 10 A CW) $\theta_{95\%}$ = 9.04°, whereas for the same heat load, its magnitude reduces considerably to 8.14° and 6.83° for D3 and D5, respectively, establishing the impact of LTV. Further, $\theta_{95\%}$ is also measured under quasi-CW condition at fixed current ($I$=10 A) and is shown in Fig. 5 (d-f). As duty cycle increases, pulsed $\theta_{95\%}$ tends towards the CW value, which is as expected. It is observed that $\theta_{95\%}$ at $I$ = 10 A increases strongly (0.16 °/K) with $\Delta T_{AZ}$ for D1 with large LTV, and weakly (0.04 – 0.06 °/K) for devices, which operate with low LTV (D3 and D5). Therefore, the temperature dependence of $\theta_{95\%}$ is strongly suppressed at high $I$ when the impact of LTV is minimized by using short resonators or high $R_f$, following the same trends observed in LCA. Further, there is large background (non-thermal, see [3]) contribution to θ95% for devices D3-D6, which makes its magnitude larger compared to that of D1. This non-thermal contribution is still an open topic of research, but may be related to differences in the lateral and longitudinal carrier density and gain profiles. Results from remaining devices from each set show consistent results, which are also included in Figure 4.

In summary, longitudinal temperature variation and carrier non-pinning at the stripe edges of broad area lasers are estimated from the spatial variation of spontaneous emission wavelength and intensity, respectively. Such carrier non-pining and lateral far field angle are experimentally correlated to the magnitude of LTV. It is demonstrated that devices with low LTV, which are fabricated either with short resonators or high front facet reflectivity show improved carrier pinning (fourfold reduced LCA) at the front facet stripe edges and narrower and less temperature-sensitive (three- to fourfold reduced) lateral far field angles, with a concomitant influence on device performance.

**Acknowledgement:**
The authors thank Prof. Dr. G. Tränkle for the close support, Dr. H. Christopher for assistance in measurements and the FBH technology teams for fabricating the devices.

**References**

1. Laurent Vaissie, Tom Steele and Paul T. Rudy, Laser Focus World, June 1, (2008)
2. P Crump, S Boldicke, C M Schultz, H Ekhteraei, H Wenzel and G Erbert, Semicond. Sci. Technol. 27, 045001 (2012)
3. Paul Crump, Mohamed Elattar, Md. Jarez Miah, Member, Michael Ekterai, Matthias M. Karow, Dominik Martin, Andre Maaßdorf, Stewart McDougall, Carlo Holly, Simon Rauch, Stefan Gruetzner, Stephan Strohmaier, and Günther Tränkle, IEEE J. Sel. Topics Quantum Electron. 28, 1501111 (2022)
4. A. Boni, P. Della Casa, D. Martin and P. Crump, Proc. 27th ISLC, TuP2.3 (2021)
5. H Wenzel, P Crump, A Pietrzak, X Wang, G Erbert and G Tränkle, New J. Phys. 12, 085007 (2010)
6. Thorben Kaul, Götz Erbert, Andreas Klehr, Andre Maaßdorf, Dominik Martin, and Paul Crump, IEEE J. Sel. Topics Quantum Electron 25, 1501910 (2019)
7. Anissa Zeghuzi, *Dissertation, Humboldt-Universität zu Berlin* (2020)

8. Paul O. Leisher, Michelle Labrecque, Kevin McClune, Elliot Burke, Daniel Renner, and Jenna Campbell, Proc. 27th ISLC, TuP2.2 (2021)
9. S. Rauch, H. Wenzel, M. Radziunas, M. Haas, G. Tränkle, and H. Zimer, Appl. Phys. Lett. 110, 263504 (2017)
10. S. Rauch, P. Modak, C. Holly and H. Zimer, IEEE International Semiconductor Laser Conference (ISLC), Santa Fe, NM, USA, 2018, pp. 1-2, doi: 10.1109/ISLC.2018.8516193
11. M. G. Peters, A. Fily, V. Rossin and A. Demir, International Semiconductor Laser Conference (ISLC), Kobe, Japan, 2016, pp. 1-2.
12. S. Arslan, H. Wenzel, J. Fricke, A. Thies, A. Ginolas, C. Stölmacker, A. Maaßdorf, B. Eppich, R. B. Swertfeger, S. K. Patra, R. J. Deri, M. C. Boiselle, D. L. Pope, P. O. Leisher, G. Tränkle and P. Crump, Proc. SPIE 12021, 120210F (2022)
13. S. Arslan, R. B. Swertfeger, J. Fricke, A. Ginolas, C. Stölmacker, H. Wenzel, P. A. Crump, S. K. Patra, R. J. Deri, M. C. Boisselle, D. L. Pope, and P. O. Leisher, Appl. Phys. Lett. 117, 203506 (2020)
14. A. F. Phillips, S. J. Sweeney, A. R. Adams and P. J. A. Thijs, IEEE Journal of Selected Topics in Quantum Electronics, vol. 5, no. 3, pp. 401-412, May-June 1999, doi: 10.1109/2944.788398.
15. Francois Girardin and Guang-Hua Duan, IEEE J. Sel. Topics Quantum Electron 3, 461 (1997)
16. Hans Wenzel, Michael Dallmer and Götz Erbert, Opt. Quant Electron 40, 379 (2008)